

Article

Alkaline Media Regulated NiFe-LDH-Based Nickel–Iron Phosphides toward Robust Overall Water Splitting

Xiaohu Xu ^{1,*}, Xinyue Yu ¹, Kaiwei Guo ¹, Lijuan Dong ^{2,*} and Xiangyang Miao ^{1,*}

¹ College of Physics and Information Engineering, Shanxi Normal University, No. 339 Taiyuroad, Xiaodian District, Taiyuan 030031, China

² Shanxi Provincial Key Laboratory of Microstructure Electromagnetic Functional Materials, Shanxi Datong University, Xingyun Street, Nanjiao District, Datong 037009, China

* Correspondence: xuxiaohu@sxnu.edu.cn (X.X.); lijuan_dong@sxdtdx.edu.cn (L.D.); xymiao@sxnu.edu.cn (X.M.)

Abstract: The search for low-cost, high-performance, and robust stability bifunctional electrocatalysts to substitute noble metals-based counterparts for overall water splitting to generate clean and sustainable hydrogen energy is of great significance and challenges. Herein, a high-efficient bifunctional nickel–iron phosphide on NiFe alloy foam (denoted as e-NFP/NFF) with 3D coral-like nanostructure was controllably constructed by means of alkali etching and the introduction of non-metallic atoms P. The unique superhydrophilic coral-like structure can not only effectively facilitate the exposure of catalytic active sites and increase the electroactive surface area, but also accelerate charge transport and bubble release. Furthermore, owing to the synergistic effect between the bicomponent of nickel–iron phosphides as well as the strong electronic interactions of the multiple metal sites, the as-fabricated catalyst behaves with excellent bifunctional performance for the hydrogen evolution reaction (overpotentials of 132 and 286 mV at 10 and 300 mA·cm^{−2}, respectively) and oxygen evolution reaction (overpotentials of 181 and 303 mV at 10 and 300 mA·cm^{−2}, respectively) in alkaline electrolytes. Impressively, cells with integrated e-NFP/NFF electrodes as a cathode and anode require only a low cell voltage (1.58 V) to drive a current density of 10 mA·cm^{−2} for overall water splitting, along with remarkable stability in long-term electrochemical durability tests. This study provides a tunable synthetic strategy for the development of efficient and durable non-noble metal bifunctional catalysts based on the construction of an elaborate structure framework and rational design of the electronic structure.

Keywords: overall water splitting; transition metal phosphide; alkaline etching; hydrogen evolution reaction; oxygen evolution reaction



Citation: Xu, X.; Yu, X.; Guo, K.; Dong, L.; Miao, X. Alkaline Media Regulated NiFe-LDH-Based Nickel–Iron Phosphides toward Robust Overall Water Splitting. *Catalysts* **2023**, *13*, 198. <https://doi.org/10.3390/catal13010198>

Academic Editor: Hao Wu

Received: 15 December 2022

Revised: 11 January 2023

Accepted: 12 January 2023

Published: 14 January 2023



Copyright: © 2023 by the authors. Licensee MDPI, Basel, Switzerland. This article is an open access article distributed under the terms and conditions of the Creative Commons Attribution (CC BY) license (<https://creativecommons.org/licenses/by/4.0/>).

1. Introduction

In the context of the serious shortage of fossil energy reserves and increasingly severe environmental pollution issues, there has been a consensus on seeking eco-friendly and sustainable clean energy alternatives to substitute traditional fuels [1,2]. Renewable energy sources, such as wind and solar energies, are limited in their development and utilization due to uneven geographical distribution and intermittent supply. Therefore, the promotion of clean and green energy should be properly integrated with the infrastructure of energy storage technologies and the transportation of raw materials for production [3–5]. Owing to its high energy density (142 MJ·kg^{−1}) and zero carbon emissions, hydrogen energy has been hailed as the perfect, ultimate clean energy carrier [6]. Compared with the traditional industrial hydrogen production technique, electrochemical water splitting (EWS) is considered a simple, environment-friendly, and high-efficiency alternative solution to generating high-purity hydrogen [7]. EWS consists of two half-cell reactions, namely, cathodic hydrogen evolution reaction (HER) and anodic oxygen evolution reaction (OER), both of which suffer from sluggish kinetics and unfavorable thermodynamics [8,9]. Therefore,

it is particularly indispensable to prepare reasonable catalysts to reduce the activation barrier and accelerate the reaction process. So far, noble metal-based catalysts, such as Pt and RuO₂/IrO₂, are still the benchmark catalysts in terms of catalytic activity toward HER and OER, respectively. Nevertheless, their high cost and scarce reserves of precious metal seriously hinder their large-scale applications [10–12]. Hence, the rational design of HER and OER bifunctional alternatives with low cost, high performance, and excellent stability is of significant importance for overall water splitting (OWS) to produce clean hydrogen energy.

Over the past decades, tremendous efforts have been devoted to the development of transition metal-based catalysts, owing to their merit of earth abundance and unique d-orbital electronic configurations, such as transition metal oxides [13,14], hydroxide [15–17], sulfides [18,19], phosphides [20,21], nitrides [18,22], and so forth. Thereinto, transition metal layered double hydroxides (LDHs) possess large specific surface area, impressive mechanical behavior, and highly tunable electrochemical/electronic properties, making them become a popular choice in terms of energy storage and conversion application. Generally, LDHs are roughly expressed by the chemical formula of M^{II}_{1-x}M^{III}_x(OH)₂(Aⁿ⁻)_{x/n}·yH₂O, where the M^{II} and M^{III} represent tunable divalent and trivalent metal cations located in the positive host layers, and the Aⁿ⁻ represents the easily exchangeable charge compensating anions in the interlayer gallery [15–17]. Their intriguing 2D-layered structure, extraordinary flexible compositions, and facile preparation methods allow them to be exploited as platforms for developing LDH-based hybrid nanoarchitectures, which is fairly favorable for further modifications of their physicochemical properties. Recently, a large number of works in the literature have reported the synthesis and application of LDHs [23,24]. For example, Chen et al. adopted a simple co-precipitation method followed by acidic etching treatment to fabricate 3D NiFe-LDH nanosheets assembly with active Fe sites to realize highly efficient OER catalytic performance [25]. Su et al. reported the synthesis of NiFeAl LDHs from electroplating sludge via a simple hydrothermal method for excellent supercapacitor performance [26]. However, due to their inferior electrical conductivity, insufficient exposed active sites, and relatively poor inherent conductivity, LDHs are yet to be regarded as high-efficiency bifunctional nanomaterials for OER and HER [16]. More importantly, the unsatisfactory long-term durability under harsh electrochemical conditions makes LDHs unable to meet the requirements of practical industrial applications [27,28]. Therefore, it is urgently desired to develop highly efficient and stable bifunctional electrocatalysts for OWS.

So far, to overcome the shortcomings of pristine LDHs, hybrid LDH-based nanoarchitectures have emerged as potential candidates for OWS. Various feasible modulation strategies have been proposed to improve the catalytic performance of pristine LDHs toward OER and HER in previous reports, including morphology modulation [28,29], interface regulation [30], defect engineering [16,17], and heteroatom doping [31–33]. Among them, the heteroatom doping has attracted more attention, as a wide variety of elements can be chosen to incorporate into the crystal lattice of the host materials, which means that the physicochemical properties of the pristine LDHs could be modulated in a large range and may be likely to be optimized at some point. A proven judicious alternative is that the introduction of non-metallic elements P can lead to the regulation of the electronic structure, the increase in electrical conductivity, and the promotion of exposed active sites. As a consequence, the heteroatom doping essentially gives rise to optimizing the adsorption energy of H and the binding energy between OER intermediates and electrocatalysts, eventually resulting in the enhanced catalytic activity of HER and OER [34]. Constructing self-supporting catalysts on some substrates with high electrical conductivity and dense pores structure has been demonstrated to play a crucial part in avoiding the agglomeration and accumulation of electrocatalysts, which is also beneficial for electrolyte permeation and promoting the electron transfer and ion diffusion in the catalytic process [29,32,35]. For instance, Chen et al. prepared an amorphous nickel–iron oxyphosphide (NiFeOP) via a facile phosphidation treatment on NiFe-LDH nanoflakes, which showed a high perfor-

mance toward both HER and OER in alkaline media [33]. Qiu et al. synthesized active iron-tuned nickel phosphide nanosheets on the carbon fiber matrix as an overall water splitting catalyst via phosphating NiFe LDHs [36]. Sun and co-workers presented a series of NiFe phosphides/sulfides/selenides on carbon cloth by heteroelement-doped NiFe-LDHs for OER and explored the reasons for the differences in their catalytic activity [37].

Bearing these discussions in mind, we herein fabricated a binder-free 3D nano-coral-like nickel-iron phosphide compound electrode on a NiFe alloy foam (marked as e-NFP/NFF) as a bifunctional electrocatalyst for OWS using a three-step hydrothermal-electrodeposition-phosphorization process. Firstly, the alkaline etching strategy is applied to metallic NiFe alloy foam, which leads to the successful construction of a hierarchically layered structure consisting of interlocking stacks of nanosheets. Secondly, NiFe-LDH nanoplates prepared by electrodeposition trigger the morphological transformation from interlaced nanosheets to stacked polyhedrons. Finally, the Ni/Fe-P bond is formed by the introduction of the nonmetallic element P through the low-temperature phosphorization route. Owing to the optimized electronic structure via element P doping, the increased electrochemically active area by unique structure and the synergy between multiple components, as expected, the superhydrophilic e-NFP/NFF achieves efficient and stable HER and OER catalytic performance at high current density in alkaline media. In addition, the e-NFP/NFF electrode only needs a cell voltage of 1.58 V to output $10 \text{ mA}\cdot\text{cm}^{-2}$ in the OWS system as well as exhibiting excellent anticurrent fluctuation.

2. Results and Discussion

As illustrated in Figure 1, e-NFP/NFF catalysts were synthesized in a three-step hydrothermal-electrodeposition-phosphorization process. First, e-NFP/NFF catalyst, a layered material consisting of hierarchically interwoven nanosheets, was in situ grown on the porous conductive NiFe alloy foam substrate (NFF) through a simple hydrothermal alkali-etching method, where NFF not only serves as a substrate, but also as a provider of metal ions. Then, when a constant voltage of -1 V was applied to the e-NFP/NFF electrode for 200 s at $30 \text{ }^\circ\text{C}$ during the electrodeposition process, NiFe-LDH precursors were synthesized on the surface of e-NFP/NFF (denoted as e-NF-LDH/NFF). Finally, to introduce the transition metal P, a facile annealing treatment with sodium hypophosphite as the P source under the flowing Ar atmosphere was conducted. The color change (from yellow to slight yellowish-green and further to black) of the NFF substrate indicated the transformation and formation of e-NFP/NFF electrocatalysts.

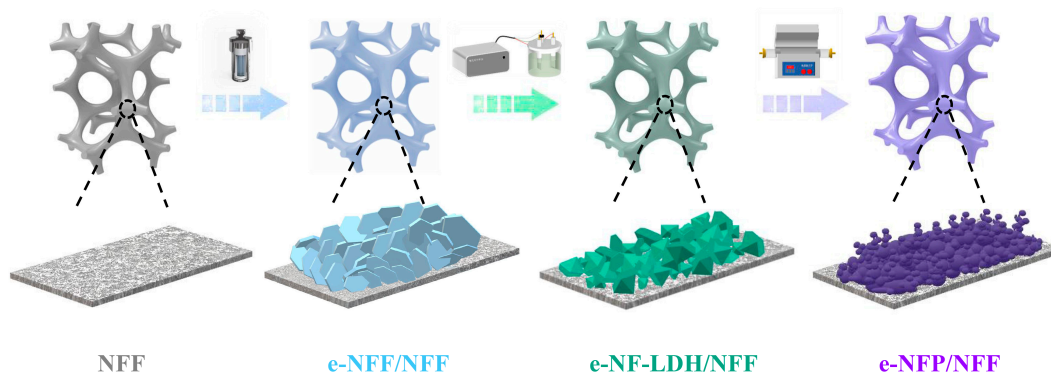


Figure 1. Schematic representation for the synthetic process of e-NFP/NFF electrodes.

The microstructure and morphology of the as-synthesized samples were characterized by field-emission scanning electron microscopy (FE-SEM) at different magnification levels. As shown in Figure 2a,b, a layered network consisting of ultrathin intertwined nanosheets with the lateral size ranging approximately from 200 to 550 nm was observed, wrapped on the NFF substrate surface during the alkali-etched process, which manifested the successful construction of hierarchical porous structures by the one-step self-regulating

alkali-etching method. In addition, we also tracked the morphology evolution with the change of the etching concentration (0, 5, 10 mM KOH). Notably, as shown in Figure S1, the prepared samples presented stacks of nanoplates with larger diameters and thicker thicknesses, as well as being adhered to by many nanospheres in the absence of alkali during the first hydrothermal treatment. With a higher concentration of alkali (10 mM KOH), irregular polyhedron structures were formed. The above results demonstrate the tunability of the morphological structures could be obtained by the kinetically controlled alkaline-etching process.

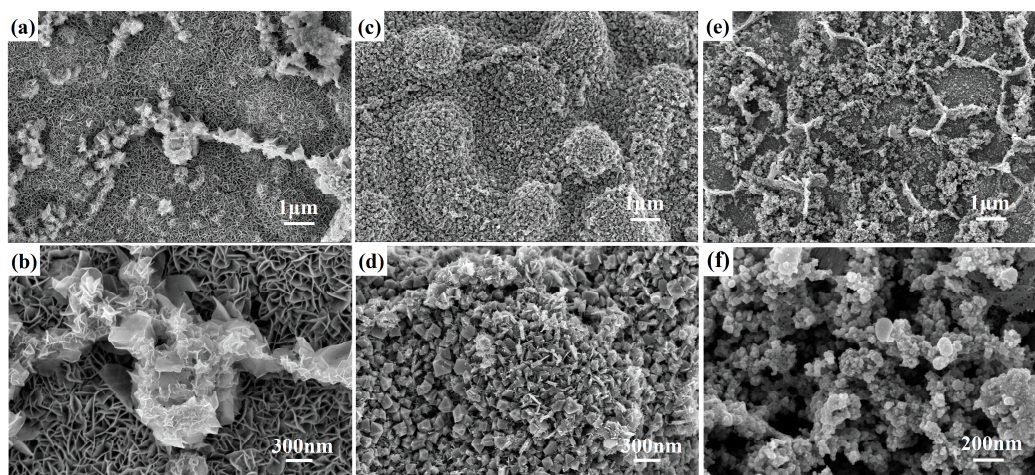


Figure 2. SEM images of e-NFF/NFF (a,b), e-NF-LDH/NFF (c,d) and e-NFP/NFF (e,f).

As shown in Figure 2c,d, the e-NF-LDH/NFF produced by the electrodeposition process based on the alkali etching strategy is different from the pristine NiFe-LDH sample composed of uniformly grown nanosheets with well-defined borders and lateral sizes of 100–300 nm (Figure S2). Close observation suggested that the self-regulated alkaline etching process endowed the e-NF-LDH/NFF with the feature of rough surface, which was covered by large amounts of irregular polyhedrons with the size of 100–200 nm and scattered sparse microspheres of 1–3 μm in diameter. After further low-temperature phosphating treatment, the electrode surface was reconstructed, and the original dense polyhedrons collapsed, leading to the formation of a three-dimensional (3D) coral-like structure assembled by numerous nanoparticles (Figure 2e,f), which can increase the electrochemically active area and be favorable for the full penetration of electrolyte and the release of bubbles, which is beneficial for the OWS reactions.

The morphology and detailed structure of the e-NFP/NFF catalyst were further investigated by using transmission electron microscopy (TEM), high-resolution transmission electron microscope (HRTEM), selected area electron diffraction (SAED), and energy dispersive spectroscopy (EDS) elemental mappings, as shown in Figure 3. The TEM images (Figure 3a) confirm the rough and porous feature of the coral-like structure formed by the accumulation of nanoparticles, which is well consistent with the FE-SEM observations. From the SAED pattern (inset in Figure 3a), a set of ordered discrete spots can be observed, which point to the exclusive pure phase of the phosphides. Furthermore, the HR-TEM image similarly corroborates the coexistence of crystalline Ni_8P_3 and FeP_4 . Five different regions were selected for observation, as illustrated in Figure 3b. The well-resolved lattice fringes with interplanar spacings of 0.260, 0.283, and 0.184 nm are indexed to the (119), (202), and (1, 2, 11) lattice planes of Ni_8P_3 (Figure 3(c2–c4)), respectively, which is in good agreement with the SAED, while the distinct lattice spacings of 0.189 and 0.252 nm are assigned to the (240) and (−132) planes of FeP_4 , respectively, (Figure 3(c1,c5)). The high-angle annular dark-field scanning TEM (HAADF-STEM) image and the corresponding elemental mappings in Figure 3d clearly show that the elements Ni, Fe, and P were uni-

formly distributed in the whole structure, further validating the successful introduction of the non-metallic element P.

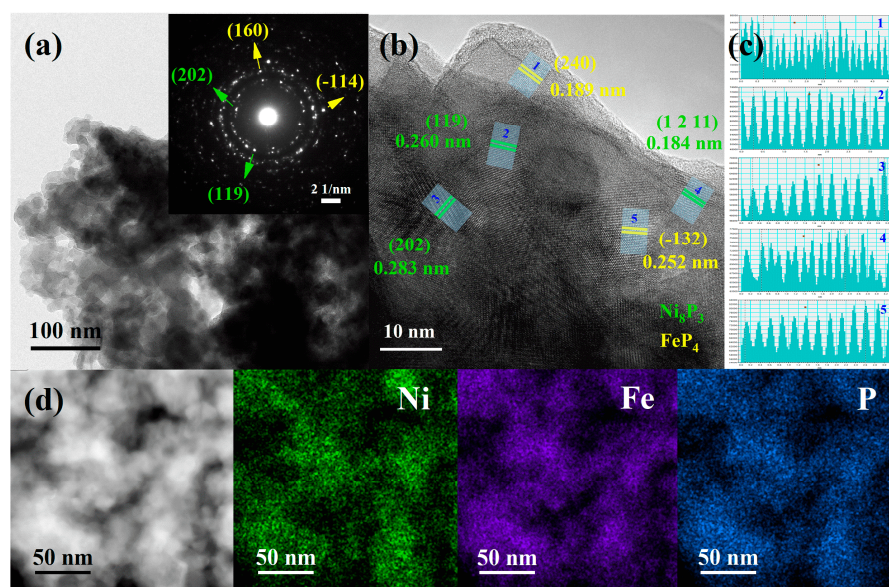


Figure 3. (a) TEM image of e-NFP scrapped from NFF; the inset image is the corresponding SAED pattern. (b) HRTEM image of e-NFP. (c1–c5) lattice spacing of e-NFP corresponding to the blue rectangles in panel b. (d) EDS elemental mapping of e-NFP.

The phases and crystal structures of as-prepared samples were further determined by X-ray diffraction (XRD). The diffraction patterns of NFF and e-NFP/NFF are shown in Figure 4, where the strong characteristic peaks located at 44.3° , 51.8° , and 76.4° were derived from the substrate of NFF, corresponding to its (111), (200), and (220) crystal planes, respectively, (PDF#38-0419). The quite weak diffraction peaks at 39.3° , 47.6° , 49.6° , and 78.4° were indexed to the (0,2,10), (300), (1,2,11) and (2,2,21) crystal planes of hexagonal Ni_8P_3 , respectively, (PDF#78-1668), while the weak peaks located at 42.3° , 48.2° , 51.1° , and 56.9° were assigned to the (052), (240), (-213), and (-261) crystal planes of orthorhombic FeP_4 , respectively, (PDF#34-0995). [38–41]. There were no diffraction peaks corresponding to other impurity phases, except for the above-mentioned diffraction peaks. Table S1 also summarizes the locations of peaks and the corresponding attributions for e-NFP/NFF. In addition, Figure S3 shows the XRD patterns comparison of the prepared samples at each step. Apparently, the absence of diffraction peaks assigned to the products after alkali etching and no typical peaks of electrodeposited NiFe LDH nanosheets could be attributed to the worse crystallinity and smaller size of the products [42,43]. To better verify the formation of NF-LDH on the e-NFF/NFF during electrodeposition, the Raman spectra of e-NFF/NFF, a-NF-LDH/NFF, and e-NF-LDH/NFF were conducted (Figure S4). Evidently, there are obvious characteristic peaks over the range of $200\sim 800\text{ cm}^{-1}$. The Raman spectrum of e-NF-LDH/NFF presented all the signals of e-NFF/NFF and a-NF-LDH/NFF [43–45]. Combined with the change of SEM images of e-NFF/NFF (Figure S2), these observations verified that NiFe-LDH was successfully loaded on the e-NFF/NFF.

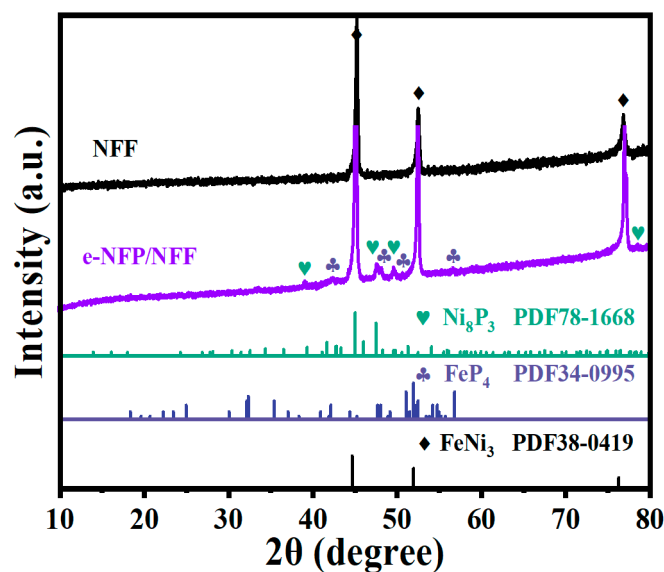


Figure 4. XRD patterns of NFF and e-NFP/NFF.

The near-surface chemical compositions and the electronic valence states of each element of the as-synthesized e-NFP/NFF were further probed by X-ray photoelectron spectroscopy (XPS). Wide-scan XPS spectra in Figure 5a showed typical signals of Ni, Fe, P, C, and O elements, which was in good accordance with the EDS results. The presence of an O 1s signal may be caused by the inevitable surface oxidation due to exposure to air. In the high-resolution Ni 2p spectrum (Figure 5b), the a-NF-LDH/NFF exhibited doublet peaks at 855.8 and 873.5 eV that could be ascribed to the Ni²⁺, while the doublet peaks at 857.2 and 875.1 eV were attributed to the Ni³⁺. In addition, two shakeup satellite peaks (denoted as “Sat.”) were observed at 862 and 879.8 eV [46,47]. After the application of the alkali etching strategy and the introduction of the non-metallic element P, the high-resolution Ni 2p spectrum of e-NFP/NFF presented two new extra peaks at 852.7 and 870 eV, which originated from the formation of Ni-P bonds [48]. Meanwhile, compared to the peaks in a-NF-LDH/NFF, it can be distinctly observed that the binding energies of Ni 2p_{1/2} and Ni 2p_{3/2} in e-NFP/NFF exhibited a slight negative shift of 0.5 and 0.3 eV, suggesting that electron transfer had occurred. Generally, the peaks shift toward lower binding energies manifested the acquirement of a higher electron density, which further confirmed that the electronic structure and coordination bonds of NiFe-LDH could be rationally regulated by the introduction of the alkali-etching strategy and the non-metallic element P. The Fe 2p core level spectrum (Figure 5c) can be divided into two pair doublets at 711.4/721.6 eV and 714.4/725.8 eV in a-NF-LDH/NFF, which belong to Fe²⁺ (Fe 2p_{3/2}/Fe 2p_{1/2}) and Fe³⁺ (Fe 2p_{3/2}/Fe 2p_{1/2}), respectively [49–51], and the shakeup satellite peak was observed at 731.8 eV. The two pairs of identical doublets in e-NFP/NFF were located at 711.6/723.5 eV and 714.5/726.8 eV, higher than those of a-NF-LDH/NFF. What is more, compared with pure NiFe-LDH catalyst, the binding energies of Ni 2p and Fe 2p in the e-NFP/NFF/NFF catalyst showed a slight negative shift and a tiny positive one, respectively, indicating the strong electronic interaction and the synergistic effect between the bicomponent of nickel–iron phosphides [52–54]. Two other sharp peaks situated at 706.7 and 719.3 eV in e-NFP/NFF were attributed to the formation of Fe-P bonds [49,55], which also strongly confirmed the successful growth of e-NFP/NFF. For the P 2p area of the e-NFP/NFF as shown in Figure 5d, the spectrum was fitted into three peaks at 129.7, 130.1, and 133.4 eV, belonging to P 2p_{3/2}, P 2p_{1/2}, and P-O, respectively [40,56]. The P-O bond may arise from the inevitable surface oxidation when exposed to air, which corresponds to the peak located at 530.5 eV in the O 1s XPS spectrum in Figure S5. The remaining two peaks at 531.3 and 532.2 eV were attributed to surface hydroxyls and surface-absorbed water, respectively [57,58].

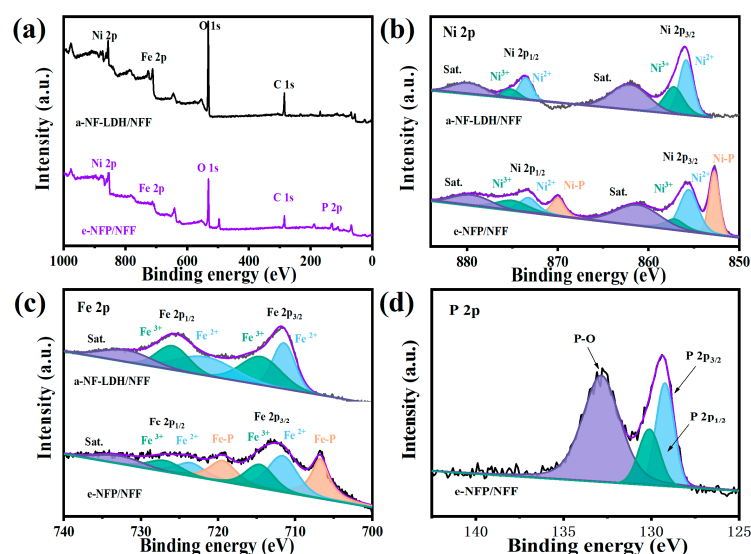


Figure 5. XPS analysis: (a) XPS survey spectra of a-NF-LDH/NFF and e-NFP/NFF; and high-resolution spectra of (b) Ni 2p, (c) Fe 2p, and (d) P 2p.

It is well known that catalyst materials possess extremely promising super-hydrophilic surfaces that facilitate the close contact between internal active sites and the external electrolyte [43,59]. To explore the hydrophilicity and wettability of the catalyst surface, the static water droplet contact angles (CA) test was performed after static loading times of 0 and 1 s, respectively, as presented in Figure S6. The bare NFF exhibited a strong hydrophobicity toward static water droplets with a contact angle of 118° , compared with the a-NF-LDH/NFF and e-NFP/NFF (ca. 0°). Since it is difficult to evaluate the contact angle of a-NF-LDH/NFF and e-NFP/NFF, the whole process of droplets contacting the electrode surfaces was also recorded in the supporting information in Videos S1–S3, respectively. Impressively, the water droplets were permeated immediately and absorbed rapidly within the droplets once in contact with the surface of a-NF-LDH/NFF and e-NFP/NFF. In this light, it is speculated that this characteristic may be attributed to the rough surface and unique 3D coral-like structure of the synthesized catalysts [60], which improved the water contact area, surface hydrophilicity, and solvent wettability, thus promoting the mass transfer process and enhancing the electrocatalytic performance [61].

Currently, alkaline water splitting is considered to be a sustainable technology for the large-scale production of hydrogen. It is worth mentioning that the design of earth-abundant, low-cost, and efficient bifunctional electrocatalysts operating in alkaline media is highly desirable. The electrocatalytic activities of the as-designed novel e-NFP/NFF electrode for HER and OER were evaluated in 1 M KOH solution with iR-correction using a standard three-electrode system, where mercury oxide electrode (Hg/HgO) and a carbon rod were utilized as the reference electrode and counter electrode, respectively. For comparison, commercial Pt/C, bare NFF, a-NF-LDH/NFF, e-NF-LDH/NFF, and a-NFP/NFF were also examined as control samples under similar conditions. Figure 6a shows the linear sweep voltammetry (LSV) curves for HER with various electrocatalysts. As expected, both Pt/C/NFF and e-NFP/NFF possessed excellent HER activity, requiring overpotentials of only 178 and 235 mV to drive $100 \text{ mA}\cdot\text{cm}^{-2}$, respectively, which were much smaller than those of other samples, including NFF (414 mV), a-NF-LDH/NFF (387 mV), e-NF-LDH/NFF (322 mV), and a-NFP/NFF (288 mV). Interestingly, it can be distinctly observed that the application of alkaline etching strategy to NFF before constructing NiFe-LDH (e-NF-LDH/NFF, green line in Figure 6a) facilitated the HER activities by the more positive shift of the overpotentials than those of pristine a-NF-LDH/NFF (blue line in Figure 6a). Combined with the above SEM comparison, it was speculated that alkaline etching was likely to modulate the morphological structure of nanomaterials by taking advantage of

their amphoteric characteristics, enriching the porosity, and increasing the electrochemically active area, finally greatly improving the HER catalytic activity. In addition, to fully investigate the effect of the alkali-etching strategy on the catalytic activity, the effects of alkali-etching concentration (Figures S7 and S8), time (Figure S9), and temperature (Figure S10) on the OWS activity were also investigated and optimized, respectively. The result revealed that the e-NFF/NFF samples with an alkali-etching concentration of 5 mM, etching time of 6 h, and temperature of 200 °C, displayed the optimal activity. Similarly, compared to e-NF-LDH/NFF (green line in Figure 6a), the final sample e-NFP/NFF (violet line in Figure 6a) exhibited a lower onset potential and a more rapid rise of current densities with the applied potential, indicating that the introduction of the nonmetallic element P also significantly enhanced HER activity, making e-NFP/NFF a promising catalyst for H₂ production through water splitting. Accordingly, we also adjusted the electrodeposition time and the dosage of NaH₂PO₂, as depicted in Figures S11–S13, in which the samples showed the best OWS performance at the addition of 0.5 g NaH₂PO₂ and deposition duration of 200 s. To allow a clearer visual comparison of the HER catalytic performance, Figure 6b exhibited the overpotentials of various samples at current densities of 50 and 100 mA·cm⁻², respectively. The excellent HER performance of e-NFP/NFF was even superior to most of the previously reported similar electrocatalysts (see Table S2 for detailed comparison).

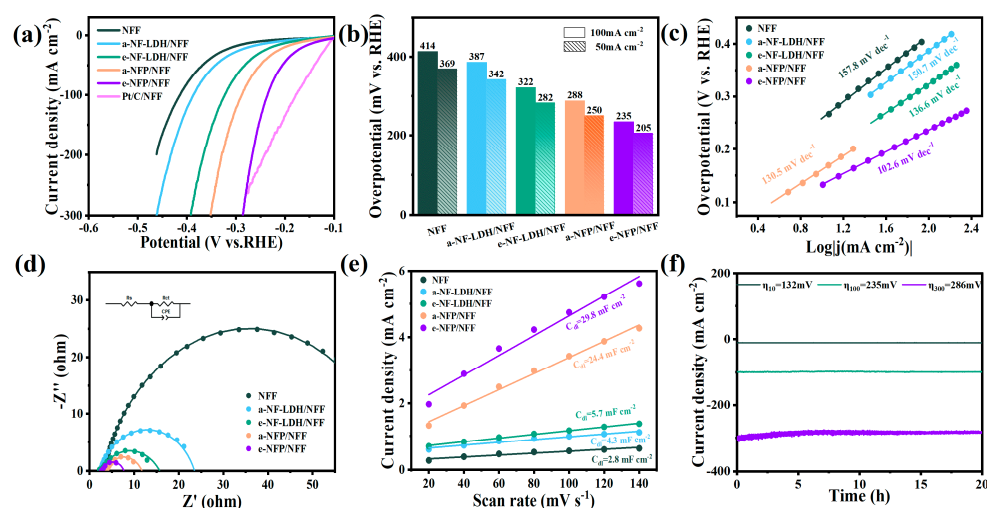


Figure 6. (a) HER polarization curves with iR-compensation for Pt/C/NFF, NFF, a-NF-LDH/NFF, e-NF-LDH/NFF, a-NFP/NFF and e-NFP/NFF; (b) overpotentials at 50 and 100 mA·cm⁻²; (c) Tafel plots of the corresponding samples; (d) Nyquist plots; (e) C_{dl} of the corresponding samples; (f) time-dependent current density curve of e-NFP/NFF at overpotentials of 132, 235, and 286 mV.

To better estimate the reaction dynamics of HER, the Tafel plot derived from the polarization curve was used as an important indicator, displayed in Figure 6c. Tafel slope of e-NFP/NFF is 102.6 mV·dec⁻¹, which is significantly lower than that of a-NFP/NFF (130.5 mV·dec⁻¹), e-NF-LDH/NFF (136.6 mV·dec⁻¹), a-NF-LDH/NFF (150.7 mV·dec⁻¹), and bare NFF (157.8 mV·dec⁻¹), confirming its more favorable HER dynamics and better inherent HER catalytic activity. Moreover, the value of the Tafel slope suggested the HER over e-NFP/NFF proceeded by a combined Volmer–Heyrovsky mechanism and the electrochemical desorption might be the rate-limiting step. In addition, electrochemical impedance spectroscopy (EIS) measurements were performed to explore the charge transfer efficiency of the as-prepared samples. According to the fitted EIS spectra (Figure 6d), the e-NFP/NFF electrode exhibited the smallest charge transfer resistance (R_{ct}), indicating a better electrical conductivity of the material, which was also in line with the analysis achieved from the Tafel plots.

Additionally, the electrochemically active surface areas (ECSAs) of those electrocatalysts could be assessed through the double-layer capacitance (C_{dl}) value, which were

calculated by cyclic voltammograms (CV) curves in the non-faraday region with different sweep rates (Figures 6e and S14). The e-NFP/NFF presented the largest slope value of $29.8 \text{ mF}\cdot\text{cm}^{-2}$ and ECSAs value of 745 cm^{-2} among the tested samples, indicating that the fabricated e-NFP/NFF with a 3D coral-like structure possessed a larger electrochemical surface area and more exposed sites for catalytic hydrogen evolution, thus improving HER activity. Turnover frequency (TOF) is also conducted to evaluate the intrinsic catalytic activity of electrocatalysts. As presented in Figure S15, the TOF value of e-NFP/NFF for HER is the highest at the same potential, significantly higher than that of a-NFP/NFF, a-NF-LDH/NFF, and e-NF-LDH/NFF, further evidencing the outstanding intrinsic activity of e-NFP/NFF.

Besides the HER performance, long-term stability is another necessary indicator to evaluate whether the electrocatalyst can be used for large-scale industrial water electrolysis. As shown in Figure S17, after 1000 cycles for HER, the current density of e-NFP/NFF exhibited a negligible decay, compared with the fresh one. Meanwhile, the durability of the e-NFP/NFF electrode and Pt/C/NFF were investigated by chronoamperometry testing curve under the constant current densities of 10 and $100 \text{ mA}\cdot\text{cm}^{-2}$ for more than 20 h, as depicted in Figures 6f and S18. In response, for e-NFP/NFF, only some tiny fluctuations were observed due to the absorption/accumulation and desorption of H_2 bubbles on the electrode surface. At a low current density, the Pt/C/NFF electrode exhibited excellent catalytic stability, similar to that of the non-noble e-NFP/NFF. Interestingly, when the current density increased up to $100 \text{ mA}\cdot\text{cm}^{-2}$, Pt/C/NFF exhibited a drastic decline in catalytic activity. It also could be seen that the e-NFP/NFF electrode survived for a long period under a large current density of $300 \text{ mA}\cdot\text{cm}^{-2}$, suggesting that the established e-NFP/NFF electrode exhibited outstanding HER activity and exceptional durability, possibly stemming from its unique coral-like structure as well as the synergistic effect among multiple components. Furthermore, after long-term HER electrolysis, the morphology and chemical composition were also characterized for the post-HER cathode. The SEM images (Figure S19a) and XRD patterns (Figure S19b) remained unchanged basically as before, indicating their ideal operational stability in alkaline media. The corresponding XPS spectra (Figure S20) after the stability test also had no obvious variation. Therefore, the above results argue that e-NFP/NFF did deserve a superior HER electrocatalyst in a basic medium.

To evaluate the potential of e-NFP/NFF electrocatalyst for OWS, we further tested the catalytic performance of the above catalysts for OER under the same experimental conditions. The corresponding iR-corrected LSV curves are shown in Figure 7a, and the overpotentials at output current densities of 50 and $100 \text{ mA}\cdot\text{cm}^{-2}$ are further summarized in Figure 7b. As a comparison, the polarization curves of benchmark RuO_2 catalyst under the same mass loading were also explored. As expected, the e-NFP/NFF catalysts exhibited excellent OER performance with the lowest overpotentials of 257 and 272 mV at current densities of 50 and $100 \text{ mA}\cdot\text{cm}^{-2}$, respectively, which were better than those of a-NF-LDH/NFF (286 and 304 mV for 50 and $100 \text{ mA}\cdot\text{cm}^{-2}$). Even at the commercially required high current density of $300 \text{ mA}\cdot\text{cm}^{-2}$, e-NFP/NFF still showed low overpotential. The Tafel plots obtained from the corresponding polarization curves were utilized to reflect the rate of oxygen evolution as well as evaluating the reaction dynamics of OER. As depicted in Figure 7c, the e-NFP/NFF presented the smallest Tafel slope of $49.6 \text{ mV}\cdot\text{dec}^{-1}$ among all the samples, suggesting the rapid OER kinetics of the e-NFP/NFF. Both the lowest overpotential and the smallest Tafel slope confirmed that the catalyst possessed excellent OER catalytic activity in alkaline solutions. The comparison of the OER catalytic performance of e-NFP/NFF catalyst with other relevant non-precious metal electrocatalysts reported in the literature is also presented in Table S3, which further points out that the OER property of the e-NFP/NFF catalyst were satisfactory. The Nyquist plot based on an EEC (Figure 7d) demonstrates that the semicircle diameter of e-NFP/NFF was the smallest among the five catalysts, indicating it possessed the lowest R_{ct} and fastest charge transfer. The impedance values of the catalysts are consistent with the trends of the LSVs and Tafel

slopes described above. It could be concluded that the potential barrier of the e-NFP/NFF was reduced by enhancing the conductivity of the catalysts, which led to the improvement of the OER efficiency. Furthermore, the TOF value of e-NFP/NFF for OER are also the largest, compared with other counterparts (Figure S21).

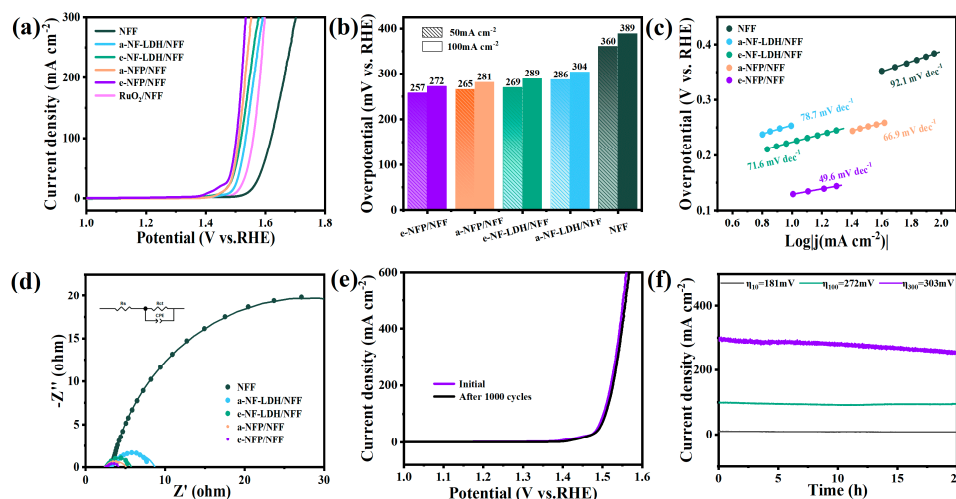


Figure 7. (a) OER polarization curves with iR -compensation for RuO_2/NFF , NFF, a-NF-LDH/NFF, e-NF-LDH/NFF, a-NFP/NFF and e-NFP/NFF; (b) Overpotentials at 50 and $100 \text{ mA}\cdot\text{cm}^{-2}$; (c) Tafel plots of the corresponding samples; (d) Nyquist plots; (e) LSV curves of e-NFP/NFF before and after 1000 cyclic test; (f) Time-dependent current density curve of e-NFP/NFF at overpotentials of 181, 272, and 303 mV.

In addition, to evaluate the stability of the e-NFP/NFF electrode for the OER, 1000 CV cycles and the long-term i - t curve were recorded. As displayed in Figure 7e, after cycling 1000 cycles, the overpotential of e-NFP/NFF to acquire $100 \text{ mA}\cdot\text{cm}^{-2}$ only increased by 6 mV. Moreover, chronoamperometric tests were performed at fixed current densities of 10, 100, and $300 \text{ mA}\cdot\text{cm}^{-2}$ for 20 h, respectively, as presented in Figure 7f. Apparently, no sharp increase or decrease was observed under the current densities of 10 and $100 \text{ mA}\cdot\text{cm}^{-2}$. When the current density was increased to $300 \text{ mA}\cdot\text{cm}^{-2}$, e-NFP/NFF showed only a slight attenuation after 20 h of OER operation. That is, the e-NFP/NFF catalyst exhibited satisfactory stability at both low and high current densities for OER. For comparison, the long-term stability of RuO_2/NFF for OER at current density of 10 and $100 \text{ mA}\cdot\text{cm}^{-2}$ over 20 h was also added as shown in Figure S22. The SEM (Figure S23a), XRD (Figure S23b), and XPS (Figure S24) spectra were also performed after long-term OER testing. The SEM images indicated that the morphology was well retained. There was a slight change in XPS, where the disappearance of nickel phosphorus bond and the weakening of iron phosphorus bond occurred. This may be caused by the surface oxidation of initial phosphides after long-term exposure to a strongly alkaline environment at high current density [41,62].

In light of the outstanding HER and OER performances, a two-electrode electrolyzer configuration for OWS was constructed by employing e-NFP/NFF as both the anode and cathode in 1 M KOH aqueous solution (labeled as e-NFP/NFF || e-NFP/NFF). As exhibited in Figure 8a, the fabricated water electrolysis device can achieve a current density of $10 \text{ mA}\cdot\text{cm}^{-2}$ with a low voltage of 1.58 V, which was close to that of the benchmark Pt/C || RuO_2 electrode (1.53 V). Furthermore, the OWS activity of e-NFP/NFF || e-NFP/NFF was also comparable to most of the recently reported results summarized in Table S4. Significantly, the e-NFP/NFF || e-NFP/NFF couple displayed excellent long-term durability, with negligible degradation of the current density after OWS testing for 20 h (Figure 8b). This undoubtedly confirmed that e-NFP/NFF is a promising bifunctional electrocatalyst with great potential for application in OWS.

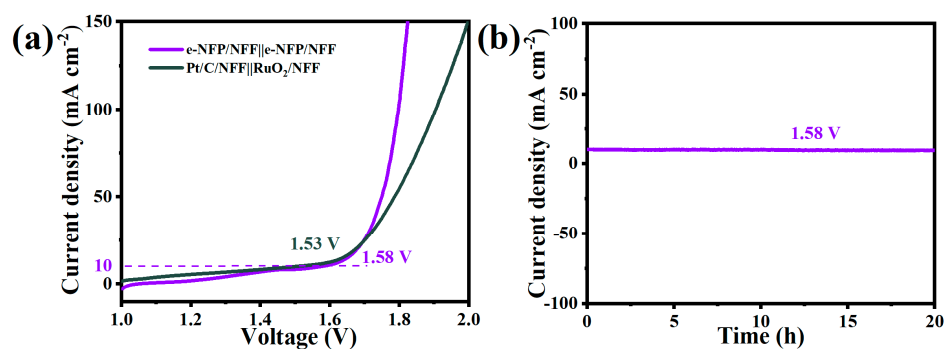


Figure 8. (a) Polarization curves of OWS for e-NFP/NFF and Pt/C | RuO₂; (b) Chronoamperometry curve of e-NFP/NFF for OWS at a voltage of 1.58 V.

3. Experimental Section

3.1. Materials

Acetone, ethanol, hydrochloric acid (HCl), potassium hydroxide (KOH), Ni(NO₃)₂·6H₂O, FeSO₄·6H₂O and sodium hypophosphite (NaH₂PO₂·H₂O) were purchased from Aladdin Chemical Reagent Co., Ltd. (Shanghai, China). NiFe alloy foam (100 mm × 100 mm × 1 mm) was bought from Kunshan Long Sheng bao Electronic Materials Co., Ltd. (Kunshan, China). Nafion (5 wt%), RuO₂, and Pt/C (20 wt%) were obtained from Shanghai Macklin Biochemical Co., Ltd. All chemicals were of analytical grade and used without further purification in the experiments. And the deionized (DI) water was used through a Millipore system.

3.2. Synthesis of the e-NFF Catalyst on NiFe Alloy Foam

First, a piece of NiFe alloy foam (1 cm × 2 cm) was washed with acetone and hydrochloric acid (3M) under ultrasonic conditions for 10 min, respectively, and then rinsed several times with DI water and ethanol to remove the surface oil and oxide layer. Afterward, the foam was immersed in 5 mM KOH solution, transferred into a 50 mL Teflon-lined steel shell autoclave, and heated to 200 °C for 6 h. Upon completion of the reaction, the resulting sample (denoted as e-NFF/NFF) was washed several times with DI water and ethanol and then dried in the oven at 60 °C. Furthermore, to explore the optimal alkaline etching conditions, the e-NFF/NFF was prepared by controlling the concentration of alkaline etching (0, 2.5, 5, 7.5, and 10 mM), the time of hydrothermal etching (3, 6, and 9 h), and the temperature of hydrothermal etching (150, 180, and 200 °C), respectively.

3.3. Synthesis of the e-NF-LDH and a-NF-LDH Catalyst on NiFe Alloy Foam

The e-NF-LDH/NFF electrode was prepared via the electrodeposition method using a typical three-electrode system on the surface of the e-NFF/NFF, where saturated calomel electrode, Pt foil, and as-prepared e-NFF/NFF were served as the reference electrode, counter electrode, and working electrode, respectively. The electrodeposition was performed at a constant voltage of −1 V for 200 s at 30 °C. The electrolyte was a mixed solution of 0.15 M Ni(NO₃)₂·6H₂O and 0.15 M FeSO₄·6H₂O. Finally, the resulting e-NF-LDH/NFF material was washed three times with ethanol and DI water and dried at 60 °C. For comparison, the a-NF-LDH catalyst was also synthesized using the same procedure, except that bare NiFe alloy foam without in situ alkali etching was used as the working electrode instead of as-prepared e-NFF/NFF. Meanwhile, the electrodeposition times (140, 200, and 260 s) were controlled to obtain the optimal catalytic performance of the e-NF-LDH/NFF and a-NF-LDH/NFF catalysts.

3.4. Synthesis of the e-NFP and a-NFP Catalyst on NiFe Alloy Foam

The e-NFP and a-NFP on NFF foam were synthesized by a simple low-temperature phosphorylation method. In a typical procedure, 0.5 g of NaH₂PO₂·H₂O and the as-prepared e-NF-LDH/NFF were placed in the upstream and the downstream region of

the tubular furnace, respectively. Subsequently, the e-NFP/NFF sample was achieved by calcination at 300 °C for 2 h with a heating rate of 2 °C·min⁻¹ under an Ar atmosphere and naturally cooling to room temperature. Based on precise measurements, the mass loading of e-NFP/NFF is 6.5 mg·cm⁻². In order to explore the optimal phosphating conditions, various electrodes were prepared by adjusting the amounts of NaH₂PO₂ (0.1, 0.5, 1 g). Additionally, the a-NFP/NFF samples were also produced in the a-NF-LDH/NFF catalyst using the same phosphorylation process.

3.5. Synthesis of Pt/C/NFF and RuO₂/NFF

For comparison, a benchmark Pt/C electrocatalyst on a NFF was fabricated by the following steps: firstly, Pt/C (13.0 mg) and Nafion solution (0.02 mL of 5 wt%) were dispersed in ethanol (0.48 mL). Secondly, the solution underwent sonication for 30 min to form a homogeneous suspension, and then 50 µL of the catalyst ink was dropped on NFF with a geometrical surface area of 0.2 cm². Finally, the Pt/C/NFF catalyst was obtained. The loading amount was ~6.5 mg·cm⁻².

Briefly, 20 mg of RuO₂ and 10 µL of 5 wt% Nafion solution were dispersed in 990 µL of anhydrous ethanol followed by ultrasonication for 20 min to form a catalyst ink. Then 65 µL of catalyst ink was loaded on NFF with a geometrical surface area of 0.2 cm² and naturally dried. Finally, the RuO₂/NFF catalyst was achieved. The mass loading was ~6.5 mg·cm⁻².

3.6. Material Characterization

The observations of surface morphology on the samples were investigated by field-emission scanning electron microscopy (FE-SEM, ZEISS Sigma 300, Taiyuan, China), high-resolution transmission electron microscopy (HR-TEM, JEM-2100, 200 kV, Shanghai, China), and corresponding selected area electron diffraction (SAED, SU8010, Shanghai, China). The crystal structure characterizations were conducted by X-ray diffractometer (XRD, Bruker D8-Advance, Taiyuan, China) equipped with a Cu K α radiation source ($\lambda = 1.5418 \text{ \AA}$). Raman characterizations were recorded by a Renishaw-inVia Raman spectrometer with 532 nm laser excitation. The near-surface chemical compositions and the electronic valence states of samples were characterized by X-ray photoelectron spectroscopy (XPS, Thermo Scientific K-Alpha, Changsha, China). The static contact angle is measured by the JY-82B Kruss DSA system at room temperature.

3.7. Electrochemical Measurements

All electrochemical data tests were performed with the CHI 760E electrochemical workstation (CH Instruments, Taiyuan, China) with a three-electrode system in an O₂ saturated 1.0 M KOH, in which an as-synthesized sample was used as working electrode, a mercury oxide electrode (Hg/HgO) as the reference one, and a carbon rod (4 mm in diameter) as the counter one, respectively. Cyclic voltammetry (CV) measurements for HER (−1.5 to −1 V (vs. Hg/HgO)) and OER (0 to 1 V (vs. Hg/HgO)) were scanning at a scanning rate of 200 mV s⁻¹, respectively. The corresponding polarization curves were acquired by using Linear Sweep Voltammetry (LSV) with a scan rate of 5 and 3 mV s⁻¹, respectively. Electrochemical impedance spectroscopy (EIS) was carried out in the frequency range of 100 KHz ~1 Hz with an amplitude potential of 5 mV. The stability tests were conducted using the chronopotentiometric method at a certain potential. In addition, the polarization curve of the OWS was measured from 1.0 to 2.0 V at a sweep rate of 5 mV s⁻¹ via a two-electrode configuration in 1 M KOH, and the chronopotentiometric curve was recorded at a constant potential of 1.58 V. The electrochemical data were not collected until the signals of working electrodes stabilized after scanning several times. All measured potentials were calibrated to the reversible hydrogen electrode (RHE) according to the following equation: $E(\text{RHE}) = E(\text{vs. Hg/HgO}) + 0.059 \times \text{pH} + 0.098$. All the above measurements were manually iR compensated and corrected using current and solution resistance. Furthermore, all experiments were repeated at least three times to ensure reliability and reproducibility.

4. Conclusions

In conclusion, with the assistance of an alkaline etching strategy and the introduction of non-metallic element P to pristine NiFe-LDH, we successfully designed a superhydrophilic 3D coral-like bi-functional e-NFP/NFF electrocatalyst on NiFe alloy foam with increased electrochemical surface area and reduced mass transfer resistance for efficient overall water splitting. By taking advantage of the strong electronic interactions between the polymetallic centers and mutual synergistic effect among the nickel–iron phosphides bicomponent, the as-prepared e-NFP/NFF electrocatalyst exhibited excellent HER and OER performance as well as robust stability both at the low (10 and 100 mA·cm⁻²) and high current densities (300 mA·cm⁻²). Furthermore, as a bifunctional electrocatalyst for OWS, only a low voltage of 1.58 V was required to drive a current density of 10 mA·cm⁻², along with remarkable stability. This work not only provides valuable insights into the construction of elaborate frameworks and the rational design of electronic structures, but also offers new perspectives for the development of highly active bifunctional electrocatalysts.

Supplementary Materials: The following supporting information can be downloaded at: <https://www.mdpi.com/article/10.3390/catal13010198/s1>, Figure S1: SEM images of e-NFF/NFF with (a) 0 mM, (b) 5 mM, and (c) 10 mM KOH treatment; Figure S2: SEM images of a-NF-LDH/NFF by electrodeposition (a) Low (b) High magnification; Figure S3: XRD patterns of (a) NFF, (b) NFF, e-NFF/NFF, a-NF-LDH/NFF, e-NF-LDH/NFF and e-NFP/NFF; Figure S4: Raman spectra of e-NFF/NFF, a-NF-LDH/NFF, and e-NF-LDH/NFF; Figure S5: XPS spectra of O 1s from the e-NFP/NFF; Figure S6: The static water droplet contact angles for bare NFF (a and b), a-NF-LDH/NFF (c and d) and e-NFP/NFF (e and f); Figure S7: (a) HER and (b) OER polarization curves of e-NFF/NFF samples synthesized with different concentration of KOH (0, 2.5, 5, 7.5, 10 mM); Figure S8: (a) HER and (b) OER polarization curves of e₁₀-NFF, e₅-NFF, e₁₀-NFF-P, e₅-NFF-P, and e-NFP; Figure S9: (a) HER and (b) OER polarization curves of e-NFF/NFF samples synthesized with different hydrothermal time (3 h, 6 h, 9 h); Figure S10: (a) HER and (b) OER polarization curves of e-NFF/NFF samples synthesized with different hydrothermal temperature (150 °C, 180 °C, 200 °C); Figure S11: (a) HER and (b) OER polarization curves of a-NF-LDH/NFF samples synthesized with different deposition time (140 s, 200 s, 260 s); Figure S12: (a) HER and (b) OER polarization curves of e-NF-LDH/NFF samples synthesized with different deposition time (140 s, 200 s, 260 s); Figure S13: (a) HER and (b) OER polarization curves of e-NFP/NFF samples synthesized with different amounts of NaH₂PO₂ (0.1, 0.5, 1 g); Figure S14: CV curves of (a) NFF, (b) a-NF-LDH/NFF, (c) e-NF-LDH/NFF, (d) a-NFP/NFF, (e) e-NFP/NFF in the non-faradaic region with different scanning rates from 20 to 140 mV·s⁻¹. (f) The ECSAs of the NFF, a-NF-LDH/NFF, e-NF-LDH/NFF, a-NFP/NFF and e-NFP/NFF; Figure S15: The potential-dependent TOF curves for HER of the a-NF-LDH/NFF, e-NF-LDH/NFF, a-NFP/NFF and e-NFP/NFF; Figure S16: Reduction peaks recorded at 0.2 V·s⁻¹. (a) a-NF-LDH/NFF, (b) e-NF-LDH/NFF, (c) a-NFP/NFF, (d) e-NFP/NFF; Figure S17: LSV curves of e-NFP/NFF for HER before and after 1000 cyclic test; Figure S18: Time-dependent current density curve of Pt/C/NFF for HER; Figure S19: (a) SEM image and (b) XRD pattern of e-NFP/NFF after HER electrolysis; Figure S20: (a) XPS full survey spectrum of e-NFP/NFF after HER electrolysis. High-resolution XPS spectrum: (b) Ni 2p, (c) Fe 2p, and (d) P 2p; Figure S21: The potential-dependent TOF curves for OER of the a-NF-LDH/NFF, e-NF-LDH/NFF, a-NFP/NFF and e-NFP/NFF; Figure S22: Time-dependent current density curve of RuO₂/NFF for OER; Figure S23: (a) SEM image and (b) XRD pattern of e-NFP/NFF after OER electrolysis; Figure S24: (a) XPS full survey spectrum of e-NFP/NFF after OER electrolysis. High-resolution XPS spectrum: (b) Ni 2p, (c) Fe 2p, and (d) P 2p; Table S1: Corresponding structure of XRD peaks in e-NFP/NFF; Table S2: Comparison of e-NFP/NFF catalyst with recently reported catalysts in HER performance in alkaline media (1 M KOH); Table S3: Comparison of e-NFP/NFF catalyst with recently reported catalysts in OER performance in alkaline media (1 M KOH); Table S4: Comparison of cell voltage of e-NFP/NFF electrocatalyst with other bifunctional electrocatalysts in alkaline media (1 M KOH); Video S1: The contact angle test procedure for bare NFF; Video S2: The contact angle test procedure for a-NF-LDH/NFF; Video S3: The contact angle test procedure for e-NFP/NFF; Video S4: The water splitting process for e-NFP/NFF || e-NFP/NFF at 10 mA·cm⁻²; Video S5: The water splitting process for e-NFP/NFF || e-NFP/NFF at 100 mA·cm⁻²; References [37,40,63–81] are cited in the Supplementary Materials.

Author Contributions: Conceptualization, X.X. and X.Y.; methodology, X.X.; software, X.Y.; validation, X.X., X.Y. and K.G.; formal analysis, X.X.; investigation, X.X. and X.Y.; resources, X.X. and X.M.; data curation, X.X. and X.Y.; writing—original draft preparation, X.X. and X.Y.; writing—review and editing, X.X. and X.Y.; visualization, X.X. and X.Y.; supervision, X.X., X.M. and L.D.; project administration, X.X.; funding acquisition, X.X. and X.Y. All authors have read and agreed to the published version of the manuscript.

Funding: This work was funded by the National Natural Science Foundation of China (No. 11974229), Applied and Basic Research Program of Shanxi Province (No. 20210302123327), and Innovation Project of Graduate Education in Shanxi Province (No. 2022Y499).

Data Availability Statement: All relevant data used in this study are presented in the form of figures and tables in published articles, and all data presented in this manuscript are available on request.

Acknowledgments: This work was supported by the National Natural Science Foundation of China (No. 11974229), Applied and Basic Research Program of Shanxi Province (No. 20210302123327), and Innovation Project of Graduate Education in Shanxi Province (No. 2022Y499). Authors thank Analysis and Measurement Center of Shanxi Normal University for the sample testing service.

Conflicts of Interest: The authors declare no conflict of interest.

References

1. Zou, X.X.; Zhang, Y. Noble metal-free hydrogen evolution catalysts for water splitting. *Chem. Soc. Rev.* **2015**, *44*, 5148–5180. [[CrossRef](#)] [[PubMed](#)]
2. Lewis, N.S.; Nocera, D.G. Powering the planet: Chemical challenges in solar energy utilization. *Proc. Natl. Acad. Sci. USA* **2006**, *103*, 15729–15735. [[CrossRef](#)]
3. Katsounaros, I.; Cherevko, S.; Zeradjanin, A.R.; Mayrhofer, K.J.J. Oxygen electrochemistry as a cornerstone for sustainable energy conversion. *Angew. Chem. Int. Ed.* **2014**, *53*, 102–121. [[CrossRef](#)] [[PubMed](#)]
4. Jacobson, M.Z. Review of solutions to global warming, air pollution, and energy security. *Energy Environ. Sci.* **2009**, *2*, 148–173. [[CrossRef](#)]
5. Dotan, H.; Landman, A.; Sheehan, S.W.; Malviya, K.D.; Shter, G.E.; Grave, D.A.; Arzi, Z.; Yehudai, N.; Halabi, M.; Gal, N.; et al. Decoupled hydrogen and oxygen evolution by a two-step electrochemical–chemical cycle for efficient overall water splitting. *Nat. Energy* **2019**, *4*, 786–795. [[CrossRef](#)]
6. Xiong, B.Y.; Chen, L.S.; Shi, J.L. Anion-Containing Noble-Metal-Free Bifunctional Electrocatalysts for Overall Water Splitting. *ACS Catal.* **2018**, *8*, 3688–3707. [[CrossRef](#)]
7. Burke, M.S.; Enman, L.J.; Batchellor, A.S.; Zou, S.H.; Boettcher, S.W. Oxygen Evolution Reaction Electrocatalysis on Transition Metal Oxides and (Oxy)hydroxides: Activity Trends and Design Principles. *Chem. Mater.* **2015**, *27*, 7549–7558. [[CrossRef](#)]
8. Gao, T.T.; Zhou, C.X.; Chen, X.J.; Huang, Z.H.; Yuan, H.Y.; Xiao, D. Surface in situ self-reconstructing hierarchical structures derived from ferrous carbonate as efficient bifunctional iron-based catalysts for oxygen and hydrogen evolution reactions. *J. Mater. Chem. A* **2020**, *8*, 18367–18375. [[CrossRef](#)]
9. Wang, K.X.; Wang, X.Y.; Li, Z.J.; Yang, B.; Ling, M.; Gao, X.; Lu, J.G.; Shi, Q.R.; Lei, L.C.; Wu, G.; et al. Designing 3d dual transition metal electrocatalysts for oxygen evolution reaction in alkaline electrolyte: Beyond oxides. *Nano Energy* **2020**, *77*, 105162. [[CrossRef](#)]
10. McCrum, I.T.; Koper, M.T.M. The role of adsorbed hydroxide in hydrogen evolution reaction kinetics on modified platinum. *Nat. Energy* **2020**, *5*, 891–899. [[CrossRef](#)]
11. Zhang, Y.K.; Wu, C.Q.; Jiang, H.L.; Lin, Y.X.; Liu, H.J.; He, Q.; Chen, S.M.; Duan, T.; Song, L. Atomic Iridium Incorporated in Cobalt Hydroxide for Efficient Oxygen Evolution Catalysis in Neutral Electrolyte. *Adv. Mater.* **2018**, *30*, 1707522. [[CrossRef](#)] [[PubMed](#)]
12. Rao, R.R.; Kolb, M.J.; Giordano, L.; Pedersen, A.F.; Katayama, Y.; Hwang, J.; Mehta, A.; You, H.; Lunger, J.R.; Zhou, H.; et al. Operando identification of site-dependent water oxidation activity on ruthenium dioxide single-crystal surfaces. *Nat. Catal.* **2020**, *3*, 516–525. [[CrossRef](#)]
13. Smith, R.D.L.; Prevot, M.S.; Fagan, R.D.; Zhang, Z.P.; Sedach, P.A.; Siu, M.K.J.; Trudel, S.; Berlinguette, C.P. Photochemical route for accessing amorphous metal oxide materials for water oxidation catalysis. *Science* **2013**, *340*, 60–63. [[CrossRef](#)] [[PubMed](#)]
14. Yang, G.Y.; Xiang, H.; Rauf, M.; Mi, H.W.; Ren, X.Z.; Zhang, P.X.; Li, Y.L. Plasma enhanced atomic-layer-deposited nickel oxide on Co₃O₄ arrays as highly active electrocatalyst for oxygen evolution reaction. *J. Power Sources* **2021**, *481*, 228925. [[CrossRef](#)]
15. Lv, L.; Yang, Z.X.; Chen, K.; Wang, C.D.; Xiong, Y.J. 2D Layered Double Hydroxides for Oxygen Evolution Reaction: From Fundamental Design to Application. *Adv. Energy Mater.* **2019**, *9*, 1803358. [[CrossRef](#)]
16. Mu, W.N.; Bao, D.C.; Chang, C. Growth of nickel vacancy NiFe-LDHs on Ni(OH)₂ nanosheets as highly efficient bifunctional electrocatalyst for overall water splitting. *Int. J. Hydrogen Energy* **2022**, *47*, 15603–15611. [[CrossRef](#)]
17. Han, X.Q.; Lin, Z.H.; He, X.Q.; Cui, L.L.; Lu, D.X. The construction of defective FeCo-LDHs by in-situ polyaniline curved strategy as a desirable bifunctional electrocatalyst for OER and HER. *Int. J. Hydrogen Energy* **2020**, *45*, 26989–26999. [[CrossRef](#)]

18. Liang, J.; Jiao, Y.; Jaroniec, M.; Qiao, S.Z. Sulfur and nitrogen dual-doped mesoporous graphene electrocatalyst for oxygen reduction with synergistically enhanced performance. *Angew. Chem.* **2012**, *124*, 11664–11668. [[CrossRef](#)]
19. He, W.J.; Wang, F.Q.; Jia, D.B.; Li, Y.; Liang, L.M.; Zhang, J.; Hao, Q.Y.; Liu, C.C.; Liu, H.; Zhao, J.L. Al-doped nickel sulfide nanosheet arrays as highly efficient bifunctional electrocatalysts for overall water splitting. *Nanoscale* **2020**, *12*, 24244–24250. [[CrossRef](#)]
20. Wang, T.Y.; Wang, C.; Jin, Y.; Sviripa, A.; Liang, J.S.; Han, J.T.; Huang, Y.H.; Li, Q.; Wu, G. Amorphous Co–Fe–P nanospheres for efficient water oxidation. *J. Mater. Chem. A* **2017**, *5*, 25378–25384. [[CrossRef](#)]
21. Chouki, T.; Machreki, M.; Emin, S. Solvothermal synthesis of iron phosphides and their application for efficient electrocatalytic hydrogen evolution. *Int. J. Hydrogen Energy* **2020**, *45*, 21473–21482. [[CrossRef](#)]
22. Han, N.; Liu, P.Y.; Jiang, J.; Ai, L.H.; Shao, Z.P.; Liu, S.M. Recent advances in nanostructured metal nitrides for water splitting. *J. Mater. Chem. A* **2018**, *6*, 19912–19933. [[CrossRef](#)]
23. Li, W.M.; Chen, S.H.; Zhong, M.X.; Wang, C.; Lu, X.F. Synergistic coupling of NiFe layered double hydroxides with Co-C nanofibers for high-efficiency oxygen evolution reaction. *Chem. Eng. J.* **2021**, *415*, 128879. [[CrossRef](#)]
24. Liu, R.; Wang, Y.Y.; Liu, D.D.; Zou, Y.Q.; Wang, S.Y. Water-Plasma-Enabled Exfoliation of Ultrathin Layered Double Hydroxide Nanosheets with Multivacancies for Water Oxidation. *Adv. Mater.* **2017**, *29*, 1701546. [[CrossRef](#)] [[PubMed](#)]
25. Peng, C.L.; Ran, N.; Wan, G.; Zhao, W.P.; Kuang, Z.Y.; Lu, Z.; Sun, C.J.; Liu, J.J.; Wang, L.Z.; Chen, H.R. Engineering Active Fe Sites on Nickel-Iron Layered Double Hydroxide through Component Segregation for Oxygen Evolution Reaction. *ChemSusChem* **2020**, *13*, 811–818. [[CrossRef](#)]
26. Liu, T.B.; Zhou, H.F.; Zhong, G.X.; Yan, X.L.; Su, X.T.; Lin, Z. Synthesis of NiFeAl LDHs from electroplating sludge and their excellent supercapacitor performance. *J. Hazard. Mater.* **2021**, *404*, 124113. [[CrossRef](#)]
27. Tomboc, G.M.; Kim, J.; Wang, Y.T.; Son, Y.C.; Li, J.H.; Kim, J.Y.; Lee, K. Hybrid layered double hydroxides as multifunctional nanomaterials for overall water splitting and supercapacitor applications. *J. Mater. Chem. A* **2021**, *9*, 4528–4557. [[CrossRef](#)]
28. Lin, Y.P.; Wang, H.; Peng, C.K.; Bu, L.M.; Chiang, C.L.; Tian, K.; Zhao, Y.; Zhao, J.Q.; Lin, Y.G.; Lee, J.M.; et al. Co-Induced Electronic Optimization of Hierarchical NiFe LDH for Oxygen Evolution. *Small* **2020**, *16*, 2002426. [[CrossRef](#)]
29. Song, D.N.; Sun, J.K.; Sun, L.J.; Zhai, S.L.; Ho, G.W.; Wu, H.; Deng, W.Q. Acidic Media Regulated Hierarchical Cobalt Compounds with Phosphorous Doping as Water Splitting Electrocatalysts. *Adv. Energy Mater.* **2021**, *11*, 2100358. [[CrossRef](#)]
30. Li, X.P.; Zheng, L.R.; Liu, S.J.; Ouyang, T.; Ye, S.; Liu, Z.Q. Heterostructures of NiFe LDH hierarchically assembled on MoS₂ nanosheets as high-efficiency electrocatalysts for overall water splitting. *Chin. Chem. Lett.* **2022**, *33*, 4761–4765. [[CrossRef](#)]
31. Yang, Z.X.; Zhang, Y.Q.; Feng, C.Q.; Wu, H.M.; Ding, Y.; Mei, H. P doped NiCoZn LDH growth on nickel foam as an highly efficient bifunctional electrocatalyst for Overall Urea-Water Electrolysis. *Int. J. Hydrogen Energy* **2021**, *46*, 25321–25331. [[CrossRef](#)]
32. Chen, S.; Duan, J.J.; Bian, P.J.; Tang, Y.H.; Zheng, R.K.; Qiao, S.Z. Three-Dimensional Smart Catalyst Electrode for Oxygen Evolution Reaction. *Adv. Energy Mater.* **2015**, *5*, 1500936. [[CrossRef](#)]
33. Chen, J.S.; Guo, Z.Z.; Luo, Y.X.; Cai, M.D.; Gong, Y.X.; Sun, S.; Li, Z.X.; Mao, C.J. Engineering Amorphous Nickel Iron Oxyphosphide as a Highly Efficient Electrocatalyst toward Overall Water Splitting. *ACS Sustain. Chem. Eng.* **2021**, *9*, 9436–9443. [[CrossRef](#)]
34. Shi, Y.M.; Li, M.Y.; Yu, Y.F.; Zhang, B. Recent advances in nanostructured transition metal phosphides: Synthesis and energy-related applications. *Energy Environ. Sci.* **2020**, *13*, 4564–4582. [[CrossRef](#)]
35. Qin, S.L.; Lei, J.L.; Xiong, Y.; Xu, X.H.; Geng, X.H.; Wang, J.H. Synthesis of Ni_{4.5}Fe_{4.5}S₈/Ni₃S₂ film on Ni₃Fe alloy foam as an excellent electrocatalyst for the oxygen evolution reaction. *RSC Adv.* **2019**, *9*, 10231–10236. [[CrossRef](#)]
36. Huang, H.W.; Yu, C.; Zhao, C.T.; Han, X.T.; Yang, J.; Liu, Z.B.; Li, S.F.; Zhang, M.D.; Qiu, J.S. Iron-tuned super nickel phosphide microstructures with high activity for electrochemical overall water splitting. *Nano Energy* **2017**, *34*, 472–480. [[CrossRef](#)]
37. Wu, X.J.; Liu, H.Z.; Li, F.S.; Lu, L.J.; Li, W.J.; Feng, L.; Sun, L.C. Exploration of electrocatalytic water oxidation properties of NiFe catalysts doped with nonmetallic elements (P, S, Se). *Int. J. Hydrogen Energy* **2021**, *46*, 38992–39002. [[CrossRef](#)]
38. Zhang, W.X.; Jia, Q.; Liang, H.; Cui, L.; Wei, D.; Liu, J.Q. Iron doped Ni₃S₂ nanorods directly grown on FeNi₃ foam as an efficient bifunctional catalyst for overall water splitting. *Chem. Eng. J.* **2020**, *396*, 125315. [[CrossRef](#)]
39. Shen, J.; Li, Q.; Zhang, W.X.; Cai, Z.Y.; Cui, L.; Liu, X.P.; Liu, J.Q. Spherical Co₃S₄ grown directly on Ni–Fe sulfides as a porous nanoplate array on FeNi₃ foam: A highly efficient and durable bifunctional catalyst for overall water splitting. *J. Mater. Chem. A* **2022**, *10*, 5442–5451. [[CrossRef](#)]
40. Yu, J.; Li, Q.Q.; Chen, N.; Xu, C.Y.; Zhen, L.; Wu, J.S.; Dravid, V.P. Carbon-Coated Nickel Phosphide Nanosheets as Efficient Dual-Electrocatalyst for Overall Water Splitting. *ACS Appl. Mater. Interfaces* **2016**, *8*, 27850–27858. [[CrossRef](#)]
41. Yan, P.X.; Hu, Y.; Shoko, E.; Isimjan, T.T.; Tian, J.N.; Yang, X.L. Hierarchical Core-Shell N-Doped Carbon@FeP₄-CoP Arrays as Robust Bifunctional Electrocatalysts for Overall Water Splitting at High Current Density. *Adv. Mater. Interfaces* **2021**, *8*, 2100065. [[CrossRef](#)]
42. Song, C.Y.; Liu, Y.; Wang, Y.C.; Tang, S.H.; Li, W.K.; Li, Q.; Zeng, J.; Chen, L.; Peng, H.C.; Lei, Y.P. Highly efficient oxygen evolution and stable water splitting by coupling NiFe LDH with metal phosphides. *Sci. China Mater.* **2021**, *64*, 1662–1670. [[CrossRef](#)]
43. Li, Y.Y.; Guo, H.R.; Zhang, Y.; Zhang, H.T.; Zhao, J.Y.; Song, R. Hollow Mo-doped NiS_x nanoarrays decorated with NiFe layered double-hydroxides for efficient and stable overall water splitting. *J. Mater. Chem. A* **2022**, *10*, 18989–18999. [[CrossRef](#)]

44. Oliver-Tolentino, M.A.; Vázquez-Samperio, J.; Manzo-Robledo, A.; González-Huerta, R.d.G.; Flores-Moreno, J.L.; Ramírez-Rosales, D.; Guzmán-Vargas, A. An Approach to Understanding the Electrocatalytic Activity Enhancement by Superexchange Interaction toward OER in Alkaline Media of Ni–Fe LDH. *J. Phys. Chem. C* **2014**, *118*, 22432–22438. [[CrossRef](#)]
45. Lai, W.; Ge, L.H.; Li, H.M.; Deng, Y.L.; Xu, B.; Ouyang, B.; Kan, E. In situ Raman spectroscopic study towards the growth and excellent HER catalysis of Ni/Ni(OH)₂ heterostructure. *Int. J. Hydrogen Energy* **2021**, *46*, 26861–26872. [[CrossRef](#)]
46. Wu, Z.C.; Zou, Z.X.; Huang, J.S.; Gao, F. NiFe₂O₄ Nanoparticles/NiFe Layered Double-Hydroxide Nanosheet Heterostructure Array for Efficient Overall Water Splitting at Large Current Densities. *ACS Appl. Mater. Interfaces* **2018**, *10*, 26283–26292. [[CrossRef](#)]
47. Jia, Y.; Zhang, L.Z.; Gao, G.P.; Chen, H.; Wang, B.; Zhou, J.Z.; Soo, M.T.; Hong, M.; Yan, X.C.; Qian, G.; et al. A Heterostructure Coupling of Exfoliated Ni-Fe Hydroxide Nanosheet and Defective Graphene as a Bifunctional Electrocatalyst for Overall Water Splitting. *Adv. Mater.* **2017**, *29*, 1700017. [[CrossRef](#)] [[PubMed](#)]
48. Zhang, M.R.; Wang, T.T.; Cao, H.Y.; Cui, S.S.; Du, P.W. Self-supported Ni₂P nanosheets on low-cost three-dimensional Fe foam as a novel electrocatalyst for efficient water oxidation. *J. Energy Chem.* **2020**, *42*, 71–76. [[CrossRef](#)]
49. Yu, J.; Zhang, T.; Sun, Y.Q.; Li, X.Y.; Li, X.Y.; Wu, B.; Men, D.; Li, Y. Hollow FeP/Fe₃O₄ Hybrid Nanoparticles on Carbon Nanotubes as Efficient Electrocatalysts for the Oxygen Evolution Reaction. *ACS Appl. Mater. Interfaces* **2020**, *12*, 12783–12792. [[CrossRef](#)]
50. Lei, X.; Qing, J.C.; Weng, L.T.; Li, S.M.; Peng, R.Z.; Wang, W.; Wang, J.L. Porous FeP/CoP heterogeneous materials as efficient alkaline oxygen evolution reaction (OER) catalysts. *New J. Chem.* **2022**, *46*, 15351–15357. [[CrossRef](#)]
51. Li, R.Q.; Wang, B.L.; Gao, T.; Zhang, R.; Xu, C.Y.; Jiang, X.F.; Zeng, J.J.; Bando, Y.; Hu, P.F.; Li, Y.L.; et al. Monolithic electrode integrated of ultrathin NiFeP on 3D strutted graphene for bifunctionally efficient overall water splitting. *Nano Energy* **2019**, *58*, 870–876. [[CrossRef](#)]
52. Sun, H.C.; Zhang, W.; Li, J.G.; Li, Z.S.; Ao, X.; Xue, K.H.; Ostrikov, K.K.; Tang, J.; Wang, C.D. Rh-engineered ultrathin NiFe-LDH nanosheets enable highly-efficient overall water splitting and urea electrolysis. *Appl. Catal. B Environ.* **2021**, *284*, 119740. [[CrossRef](#)]
53. Cui, H.; Liao, H.X.; Wang, Z.L.; Xie, J.P.; Tan, P.F.; Chu, D.W.; Jun, P. Synergistic electronic interaction between ruthenium and nickel-iron hydroxide for enhanced oxygen evolution reaction. *Rare Met.* **2022**, *41*, 2606–2615. [[CrossRef](#)]
54. Chen, Q.Q.; Hou, C.C.; Wang, C.J.; Yang, X.; Shi, R.; Chen, Y. Ir⁴⁺-Doped NiFe LDH to expedite hydrogen evolution kinetics as a Pt-like electrocatalyst for water splitting. *Chem. Commun.* **2018**, *54*, 6400–6403. [[CrossRef](#)] [[PubMed](#)]
55. Yan, Y.; Xia, B.Y.; Ge, X.M.; Liu, Z.L.; Fisher, A.; Wang, X. A Flexible Electrode Based on Iron Phosphide Nanotubes for Overall Water Splitting. *Chem. Eur. J.* **2015**, *21*, 18062–18067. [[CrossRef](#)]
56. Zhu, Y.P.; Xu, X.Y.; Su, H.; Liu, Y.P.; Chen, T.H.; Yuan, Z.Y. Ultrafine Metal Phosphide Nanocrystals in Situ Decorated on Highly Porous Heteroatom-Doped Carbons for Active Electrocatalytic Hydrogen Evolution. *ACS Appl. Mater. Interfaces* **2015**, *7*, 28369–28376. [[CrossRef](#)]
57. Xiao, C.L.; Gaddam, R.R.; Wu, Y.L.; Sun, X.M.; Liang, Y.; Li, Y.B.; Zhao, X.S. Improvement of the electrocatalytic performance of FeP in neutral electrolytes with Fe nanoparticles. *Chem. Eng. J.* **2021**, *408*, 127330. [[CrossRef](#)]
58. Hu, F.; Wang, H.Y.; Zhang, Y.; Shen, X.C.; Zhang, G.H.; Pan, Y.B.; Miller, J.T.; Wang, K.; Zhu, S.L.; Yang, X.J.; et al. Designing Highly Efficient and Long-Term Durable Electrocatalyst for Oxygen Evolution by Coupling B and P into Amorphous Porous NiFe-Based Material. *Small* **2019**, *15*, 1901020. [[CrossRef](#)]
59. Zhang, H.T.; Guo, H.R.; Zhang, Y.; Zhao, J.Y.; Li, Y.Y.; Li, X.P.; Ren, J.K.; Song, R. Metal–Organic Framework-Derived Multidimensional Hierarchical Assembling Body with a Superhydrophilic and Superaerophobic Surface Toward Efficient Electrochemical Overall Water Splitting. *ACS Sustain. Chem. Eng.* **2022**, *10*, 6402–6413. [[CrossRef](#)]
60. Yu, H.Y.; Liang, H.O.; Bai, J.; Li, C.P. Controllable growth of coral-like CuInS₂ on one-dimensional SiO₂ nanotube with superhydrophilicity for enhanced photocatalytic hydrogen evolution. *Int. J. Hydrogen Energy* **2022**, *47*, 28410–28422. [[CrossRef](#)]
61. Feng, X.T.; Jiao, Q.Z.; Dai, Z.; Dang, Y.L.; Suib, S.L.; Zhang, J.T.; Zhao, Y.; Li, H.S.; Feng, C.H.; Li, A. Revealing the effect of interfacial electron transfer in heterostructured Co₉S₈@NiFe LDH for enhanced electrocatalytic oxygen evolution. *J. Mater. Chem. A* **2021**, *9*, 12244–12254. [[CrossRef](#)]
62. Luo, X.; Ji, P.X.; Wang, P.Y.; Cheng, R.L.; Chen, D.; Lin, C.; Zhang, J.N.; He, J.W.; Shi, Z.H.; Li, N.; et al. Interface Engineering of Hierarchical Branched Mo-Doped Ni₃S₂/Ni_xP_y Hollow Heterostructure Nanorods for Efficient Overall Water Splitting. *Adv. Energy Mater.* **2020**, *10*, 1903891. [[CrossRef](#)]
63. Wei, X.J.; Zhang, Y.H.; He, H.C.; Peng, L.; Xiao, S.H.; Yao, S.R.; Xiao, P. Carbon-incorporated porous honeycomb NiCoFe phosphide nanospheres derived from a MOF precursor for overall water splitting. *Chem. Commun.* **2019**, *55*, 10896–10899. [[CrossRef](#)] [[PubMed](#)]
64. Hu, F.; Zhang, Y.; Shen, X.C.; Tao, J.Y.; Yang, X.W.; Xiong, Y.J.; Peng, Z.M. Porous amorphous NiFeO_x/NiFeP framework with dual electrocatalytic functions for water electrolysis. *J. Power Sources* **2019**, *428*, 76–81. [[CrossRef](#)]
65. Wu, Y.Q.; Tao, X.; Qing, Y.; Xu, H.; Yang, F.; Luo, S.; Tian, C.H.; Liu, M.; Lu, X.H. Cr-Doped FeNi-P Nanoparticles Encapsulated into N-Doped Carbon Nanotube as a Robust Bifunctional Catalyst for Efficient Overall Water Splitting. *Adv. Mater.* **2019**, *31*, 1900178. [[CrossRef](#)] [[PubMed](#)]
66. Bu, F.X.; Chen, W.S.; Aly Aboud, M.F.; Shakir, I.; Gu, J.J.; Xu, Y.X. Microwave-assisted ultrafast synthesis of adjustable bimetal phosphide/graphene heterostructures from MOFs for efficient electrochemical water splitting. *J. Mater. Chem. A* **2019**, *7*, 14526–14535. [[CrossRef](#)]

67. Shin, H.J.; Park, S.W.; Kim, D.W. Highly active and stable electrocatalytic transition metal phosphides (Ni₂P and FeP) nanoparticles on porous carbon cloth for overall water splitting at high current density. *Int. J. Energy Res.* **2020**, *44*, 11894–11907. [[CrossRef](#)]
68. Xuan, C.J.; Wang, J.; Xia, W.W.; Peng, Z.K.; Wu, Z.X.; Lei, W.; Xia, K.D.; Xin, H.L.; Wang, D.L. Porous Structured Ni-Fe-P Nanocubes Derived from a Prussian Blue Analogue as an Electrocatalyst for Efficient Overall Water Splitting. *ACS Appl. Mater. Interfaces* **2017**, *9*, 26134–26142. [[CrossRef](#)]
69. Hei, J.C.; Xu, G.C.; Wei, B.; Zhang, L.; Ding, H.; Liu, D. NiFeP nanosheets on N-doped carbon sponge as a hierarchically structured bifunctional electrocatalyst for efficient overall water splitting. *Appl. Surf. Sci.* **2021**, *549*, 149297. [[CrossRef](#)]
70. Liu, J.; Wang, J.S.; Zhang, B.; Ruan, Y.J.; Lv, L.; Ji, X.; Xu, K.; Miao, L.; Jiang, J.J. Hierarchical NiCo₂S₄@NiFe LDH Heterostructures Supported on Nickel Foam for Enhanced Overall-Water-Splitting Activity. *ACS Appl. Mater. Interfaces* **2017**, *9*, 15364–15372. [[CrossRef](#)]
71. Ji, P.X.; Jin, H.H.; Xia, H.L.; Luo, X.; Zhu, J.K.; Pu, Z.H.; Mu, S.C. Double Metal Diphosphide Pair Nanocages Coupled with P-doped Carbon for Accelerated Oxygen and Hydrogen Evolution Kinetics. *ACS Appl. Mater. Interfaces* **2020**, *12*, 727–733. [[CrossRef](#)] [[PubMed](#)]
72. Zhang, H.J.; Li, X.P.; Hähnel, A.; Naumann, V.; Lin, C.; Azimi, S.; Schweizer, S.L.; Maijenburg, A.W.; Wehrspohn, R.B. Bifunctional Heterostructure Assembly of NiFe LDH Nanosheets on NiCoP Nanowires for Highly Efficient and Stable Overall Water Splitting. *Adv. Funct. Mater.* **2018**, *28*, 1706847. [[CrossRef](#)]
73. Ibraheem, S.; Chen, S.G.; Li, J.; Li, W.; Gao, X.Y.; Wang, Q.M.; Wei, Z.D. Three-Dimensional Fe,N-Decorated Carbon-Supported NiFeP Nanoparticles as an Efficient Bifunctional Catalyst for Rechargeable Zinc-O₂ Batteries. *ACS Appl. Mater. Interfaces* **2019**, *11*, 699–705. [[CrossRef](#)] [[PubMed](#)]
74. Wu, Y.H.; Yi, Y.Y.; Sun, Z.T.; Sun, H.; Guo, T.Q.; Zhang, M.H.; Cui, L.F.; Jiang, K.; Peng, Y.; Sun, J.Y. Bimetallic Fe-Ni Phosphide Carved Nanoframes toward Efficient Overall Water Splitting and Potassium-Ion Storage. *Chem. Eng. J.* **2020**, *390*, 124515. [[CrossRef](#)]
75. Stern, L.-A.; Feng, L.G.; Song, F.; Hu, X.L. Ni₂P as a Janus catalyst for water splitting: The oxygen evolution activity of Ni₂P nanoparticles. *Energy Environ. Sci.* **2015**, *8*, 2347–2351. [[CrossRef](#)]
76. Ren, J.T.; Hu, Z.P.; Chen, C.; Liu, Y.P.; Yuan, Z.Y. Integrated Ni₂P nanosheet arrays on three-dimensional Ni foam for highly efficient water reduction and oxidation. *J. Energy Chem.* **2017**, *26*, 1196–1202. [[CrossRef](#)]
77. Zhang, F.S.; Wang, J.W.; Luo, J.; Liu, R.R.; Zhang, Z.M.; He, C.T.; Lu, T.B. Extraction of nickel from NiFe-LDH into Ni₂P@NiFe hydroxide as a bifunctional electrocatalyst for efficient overall water splitting. *Chem. Sci.* **2018**, *5*, 1075–1394. [[CrossRef](#)]
78. Zhang, C.; Xie, Y.C.; Deng, H.; Zhang, C.; Su, J.-W.; Dong, Y.; Lin, J. Ternary nickel iron phosphide supported on nickel foam as a high-efficiency electrocatalyst for overall water splitting. *Int. J. Hydrogen Energy* **2018**, *43*, 7299–7306. [[CrossRef](#)]
79. Chang, C.P.; Zhu, S.L.; Liu, X.Y.; Chen, Y.M.; Sun, Y.Z.; Tang, Y.; Wan, P.Y.; Pan, J.Q. One-Step Electrodeposition Synthesis of Bimetal Fe- and Co-Doped NiPi/P for Highly Efficient Overall Water Splitting. *Ind. Eng. Chem. Res.* **2021**, *60*, 2070–2078. [[CrossRef](#)]
80. Yan, Y.T.; Lin, J.H.; Bao, K.; Xu, T.X.; Qi, J.L.; Cao, J.; Zhong, Z.X.; Fei, W.D.; Feng, J.C. Free-standing porous Ni₂P-Ni₅P₄ heterostructured arrays for efficient electrocatalytic water splitting. *J. Colloid Interface Sci.* **2019**, *552*, 332–336. [[CrossRef](#)]
81. Li, M.; Li, S.; Wang, J.L.; Wang, C.R.; Li, W.; Chu, P.K. NiFeP nanoflakes composite with CoP on carbon cloth as flexible and durable electrocatalyst for efficient overall water splitting. *Nanotechnology* **2019**, *30*, 485402. [[CrossRef](#)] [[PubMed](#)]

Disclaimer/Publisher’s Note: The statements, opinions and data contained in all publications are solely those of the individual author(s) and contributor(s) and not of MDPI and/or the editor(s). MDPI and/or the editor(s) disclaim responsibility for any injury to people or property resulting from any ideas, methods, instructions or products referred to in the content.